Density matrices of the excited H ($n=2$ and 3) atoms formed in 25–100-keV proton-helium charge-transfer collisions

Ashok Jain and C. D. Lin
Physics Department, Cardwell Hall, Kansas State University, Manhattan, Kansas 66506

W. Fritsch
Bereich Kern- und Strahlenphysik Hahn-Meitner-Institut für Kernforschung, Berlin G.m.B.H., D-1000 Berlin 39, West Germany
(Received 14 April 1987)

We present *ab initio* calculations for the differential and integrated (over impact parameters) density matrices of the excited hydrogen atoms ($n=2$ and 3 manifolds) formed in 25–100-keV proton-helium charge-transfer collisions. The transition amplitudes for excited states are determined in a modified two-center atomic-orbital-expansion approach within the close-coupling treatment. The target helium atom is described in a one-electron picture. The calculated partial (nlm) and total charge-transfer cross sections are in good agreement with earlier theoretical and experimental data in this energy range. From the scattering amplitudes, the integrated density matrix and its various first-order moments for the $n=3$ manifold are compared with recent measurements. From the three-dimensional charge-density plots, it is illustrated that the captured electron lags behind the projectile in the present energy range. From the impact-parameter-dependent density-matrix analysis, an approximate "classical" picture of the captured electron is presented.

I. INTRODUCTION

There has been a considerable number of experimental studies in the measurements of total and partial capture cross sections into the $n=2$ and 3 excited states of hydrogen produced in the proton-helium collisions from low[1–4] ($E<25$ keV) to intermediate[5–11] ($25<E<100$ keV) energies. In this paper we are concerned only with the intermediate-energy region ($v/v_e \sim 1-2$ a.u., where v is the velocity of the projectile and v_e is the velocity of the bound electron). Recently, Kimura[12] and Kimura and Lin[13] have summarized earlier studies (both experimental and theoretical) on the proton-helium inelastic scattering in the low- and intermediate-energy regimes.

Measurements of total charge-transfer cross sections alone for this system are no longer of great interest. Instead, measurements of capture cross sections into the nlm sublevels are of more interest for a deeper understanding of the collision dynamics. Experimentally, it is very difficult to measure absolute partial cross sections accurately: Significant errors may be introduced due to uncertainties of absolute calibration as well as by cascade feeding of the lower n (2 or 3) levels from higher ($n=4$, etc.) states. Theoretically, in a close-coupling-type (with atomic or molecular bases) approach, in this energy region, it is hard to obtain converged cross sections for the nlm sublevels due to significant couplings with excitation and ionization channels.

A knowledge of partial nlm capture cross sections will determine the polarization or angular correlation parameters, which provide a better means of checking our understanding of the details of the charge-transfer mechanism. Very recently Hippler *et al.*[9] have measured alignment A_{20} parameters for the excited $n=2$ state of the H atoms following a charge-exchange process of protons with He in the energy regions of 1–5 keV and 35–300 keV. For the $n=3$ manifold, Brower and coworkers[11] have measured the absolute partial $3lm$ relative cross sections in the energy range of 30–80 keV; these measurements include effects from cascading by actually measuring the $n=4$ populations. In the 1970's, several measurements were carried out on the nl subshell ($n=1$, 2, and 3) cross sections for the p-He capture process at intermediate energies.[5–8]

A complete quantum-mechanical description of a scattering process can be determined from the full scattering amplitudes, or equivalently, the full density matrix. The density-matrix formalism provides a complete characterization of collisionally produced excited atoms.[14] For a given nl atomic level, an equivalent description[15] of the alignment (shape) and the orientation (rotation) of the charged cloud which can be measured from the polarization of the emitted radiation is given. In the case of excited hydrogenic levels, the degenerate energy levels can be excited coherently in an electron capture experiment. Since the spin-orbit interaction time is large enough ($\sim 10^{-9}$ s) compared with the collision time ($\sim 10^{-16}$ s), the coupling of different degenerate l sublevels within an n shell, due to long-range Stark mixing, is very important.

For hydrogenic excited final atomic states, the full density matrix within a given n manifold can be deduced experimentally by measuring the four Stokes parameters of the emitted radiation as a function of an applied external electric field. The diagonal density-matrix elements correspond to the cross section of a particular nlm sublevel, while the off-diagonal matrix elements come from the coherences or the phase differences of these magnetic substates. In case of axially symmetric collisions with respect to the incoming-beam axis,

coherent excitation is allowed only between states with the same projection quantum number (m) of the total angular momentum along this axis of quantization.

Very recently, there have been several measurements to determine the full density matrix H ($n=3$) atoms formed in p-He collisions in the range 30–80 keV by Havener *et al.*[16–18] and Westerveld.[19] Earlier the coherent excitations of angular momentum levels in the hydrogen atoms formed after the capture event have been studied, employing different techniques: for example, the s-d coherences in the $n=4$ H atoms formed in p-He collisions by Dahaes and Singer[20] by observing the quantum beats in the emitted radiation; the s-p coherences in $n=2$ H atoms created in p-He collisions by Selin *et al.*[21] by applying an electric field of fixed magnitude parallel or antiparallel to the beam direction; and coherences in the $n=3$ H atoms formed in p-He collisions by Havener *et al.*[16–18] and Westerveld[19] by measuring the optical signals emitted from within a collision cell as a function of electric fields applied within the cell.

From the analysis of the experimentally determined density matrix, a large dipole moment (arising from the coherences between real, off-diagonal density-matrix elements) of the $n=3$ excited H state was observed.[16] The positive values of the dipole moment in the energy range 40–80 keV indicated that the center of electron cloud distribution lags behind the projectile. In a subsequent observation by Havener *et al.* the flow pattern of the current distribution (arising from the coherences between imaginary, off-diagonal density-matrix elements) of the captured electron was plotted in the collision plane:[17,18] This graph along with an effective velocity vector $\langle \mathbf{L}\times\mathbf{A}\rangle_{z,s}$ (see below for definition) suggested that the direction of the current reverses sign around 80 keV impact energy. The findings of these experimental studies were confirmed qualitatively by Burgdorfer and Dube[22] by calculating the $n=3$ dipole moment and the vector $\langle \mathbf{L}\times\mathbf{A}\rangle_{z,s}$ in the continuum-distorted-wave (CDW) approximation. On the basis of these density-matrix parameters they[22] presented a "classical" orbital picture of the captured electron.

In this paper we are concerned with the density matrices of the $n=2$ and 3 manifolds for the excited H atoms formed in p-He collisions at 25–100 keV. Both integrated and the differential (impact-parameter-dependent) density matrices are discussed in this energy range. The comparison of our results will be made with the density matrices determined experimentally by Havener *et al.*[16–18] and Westerveld.[19] There are certain difficulties in getting these experimental data from the numerical fitting procedure for obtaining 14 unknown density-matrix components. Only the dominant density-matrix elements are accurate within reasonable error bar; the smaller elements (both diagonal and off-diagonal) of the density matrix seem to involve large (but unknown) errors. However, their most recent efforts to determine these parameters are not affected in the same way as they did in Refs. 16–18.[19]

In order to extract physically meaningful observable quantities from the full density matrix for a given principal quantum number, several different interpretations or parametrizations of the density matrix have been suggested: (1) alignment and orientation tensors as constructed and discussed by Fano and Macek;[15] (2) electric and magnetic multipole moment operators and their time derivatives as given by Gabrielse and Band;[23] (3) for the H atom, which belongs to the O_4 symmetry group, Burgdorfer[24] considered the usual **r**, **p**, and **L** operators to parametrize the hydrogen density matrix for a given n manifold in terms of the constants of motion such as the Runge-Lenz vector **A** and the angular momentum **L**; and (4) recently, another way to look into the physical meaning of various coherences between the density-matrix elements is proposed via the electron cloud probability and current distribution functions.[17,18] In the present paper we have used the last two [(3) and (4)] parametrization techniques of the density matrix, i.e., by calculating various first-order moments and plotting the three-dimensional and contour graphs for the probability and current distributions. In addition, we have extended this parametrization as function of impact parameter b, which provides a more transparent picture of the transfer mechanism in the present p-He collisions.

In order to evaluate the scattering amplitudes as function of impact parameter for each channel and impact energy, we used the modified two-center atomic-orbital (AO) -expansion method (the so-called AO+ method), in which the extra terms in the AO expansion represent approximately the molecular effects (important at small impact parameters for lower energies) and excitation and ionization channels (which affect the large impact-parameter probability at intermediate impact energies).[25] The importance of these pseudostates will be demonstrated in Sec. IV, where the convergence of the capture probabilities is tested with respect to the size of the basis set on each center. However, the choice of the AO+basis depends upon the situation where a particular channel is important (e.g, molecular effects at low energies, excitation and/or ionization channels at intermediate energies).

A preliminary report of this work has been published earlier.[26] In the next section we summarize the method of determining the scattering amplitudes and in Sec. III we give details of the density matrix and its parametrization. Section IV and its various subsections are devoted to the results and their discussion, while Sec. V presents our concluding remarks. Atomic units are used throughout unless otherwise specified.

II. THE AO+ METHOD

The conventional two-center atomic-orbital-expansion (AOE) method, in which the time-dependent electronic wave function is expanded in terms of traveling AO's at the projectile and the target centers, is generally valid at large impact parameters and therefore in a determination of total cross sections, successful only in restricted energy regions. Molecular-orbital (MO) features at small internuclear distances and inelastic transitions occurring at small impact parameters cannot be represented by the AOE techniques. At small impact velocities ($v/v_e \ll 1$

TABLE I. Orbital exponents of the Slater-type orbital (STO) basis functions including pseudostates, and the energy eigenvalues E_i obtained by diagonalizing the one-electron projectile and target Hamiltonians, respectively.

	Projectile			Target	
State	Exponent	Energy (a.u.)	State	Exponent	Energy (a.u.)
1s	1.0	−0.500	1s	1.453	−0.9042
2s	1.0	−0.125	1s	2.78	−0.1548
2p	1.0	−0.125	1s	1.50	−0.0423
3s	1.0	−0.056	1s	0.50	0.4136
3p	1.0	−0.056	2s	0.25	5.4652
3d	1.0	−0.056	2p	1.194	−0.1238
1s	1.5	0.078			
1s	0.5	1.772			

a.u.) the MO features dominate the scattering and the AOE prescription fails.[25] One possible remedy to account for the small b scattering in the AOE method is to employ a three-center AOE model.[27] This, however, is quite difficult from a numerical standpoint because of the need to evaluate three-center integrals. Alternatively, in the AO+ method,[28] tighter united-atom (UA) orbitals are placed at each center. By orthogonalizing these UA orbitals to the low-lying separated-atom (SA) orbitals, the eigenvalues lie in the continuum. But at small internuclear separations, these pseudostates are capable of reproducing the correct MO behavior.

In the intermediate-energy region ($v/v_e \sim 1-2$ a.u.), the collision is fast for a predominantly quasimolecular development of the system but too slow for approximating the transient quasistationary states of the collision system by undistorted AO's. In this energy range, excitation and ionization processes may influence the capture channels significantly. In the AO+ expansion, pseudostates giving the approximate energy spectrum for the discrete (excitation energies) and some discrete representation of continuum (ionization) states[29] can be included in order to exploit fully the AO+ method at intermediate energies. In the present calculations we have chosen an AO+ basis set which gives a satisfactory description of the total and partial cross sections in the whole energy region considered here.

Here, for the charge-transfer reaction,

$$p+\mathrm{He}(1s^2)=\mathrm{H}(nlm)+\mathrm{He}^+(n'l'm') , \quad (1)$$

the two-center electronic Hamiltonian H_{el} for the active electron with kinetic-energy operator K, is written as

$$H_{\mathrm{el}}=K+V_P(\mathbf{r}_P)+V_T(\mathbf{r}_T) , \quad (2)$$

where the interaction potential with the projectile proton $[V_P(\mathbf{r}_P)]$ is simply $-1/r_P$, and with the target, the model potential is taken to be[30]

$$V_T(r)=-1/r-1/r[(1+1.665r)\exp(-3.36r)] . \quad (3)$$

Notice that the two-electron target system (He) is treated here as a one-electron system in a model potential [Eq. (3)] approach. Thus the electron-electron interaction is included partially only via the model potential of Eq. (3). By expressing the ground-state wave functions of the helium atom as a linear combination of 1s Slater orbitals with exponents 1.453 and 2.78 (see also Table I), this model potential [Eq. (3)] gives a binding energy of −0.9041 a.u. which is very close to the experimental value of −0.903 56 a.u.

In the semiclassical approximation, the time-dependent Schrödinger equation for the collision system

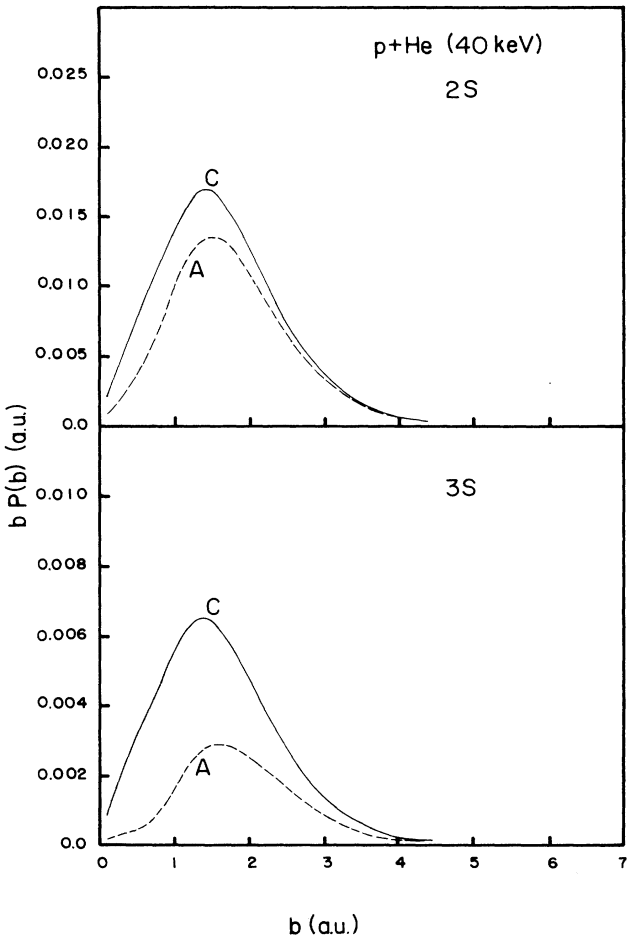

FIG. 1. Capture probability multiplied by the impact parameter vs impact parameter for H(2s,3s) transfer channels at 40 keV collision energy. Curve A, 12-state (no pseudostate) calculation; curve C, 19-state calculation.

is given by

$$(H_{el}-i\partial/\partial t)\Psi=0 , \quad (4)$$

where the total wave function of the electron is expanded as follows:

$$\Psi=\sum_i a_i^T\phi_i(\mathbf{r}_T)+\sum_j a_j^P\phi_j(\mathbf{r}_P) . \quad (5)$$

Here the $\phi_i(\mathbf{r}_T)$ and $\phi_j(\mathbf{r}_P)$ are, respectively, the traveling target and traveling projectile atomic orbitals with appropriate plane-wave translational factors. In Table I

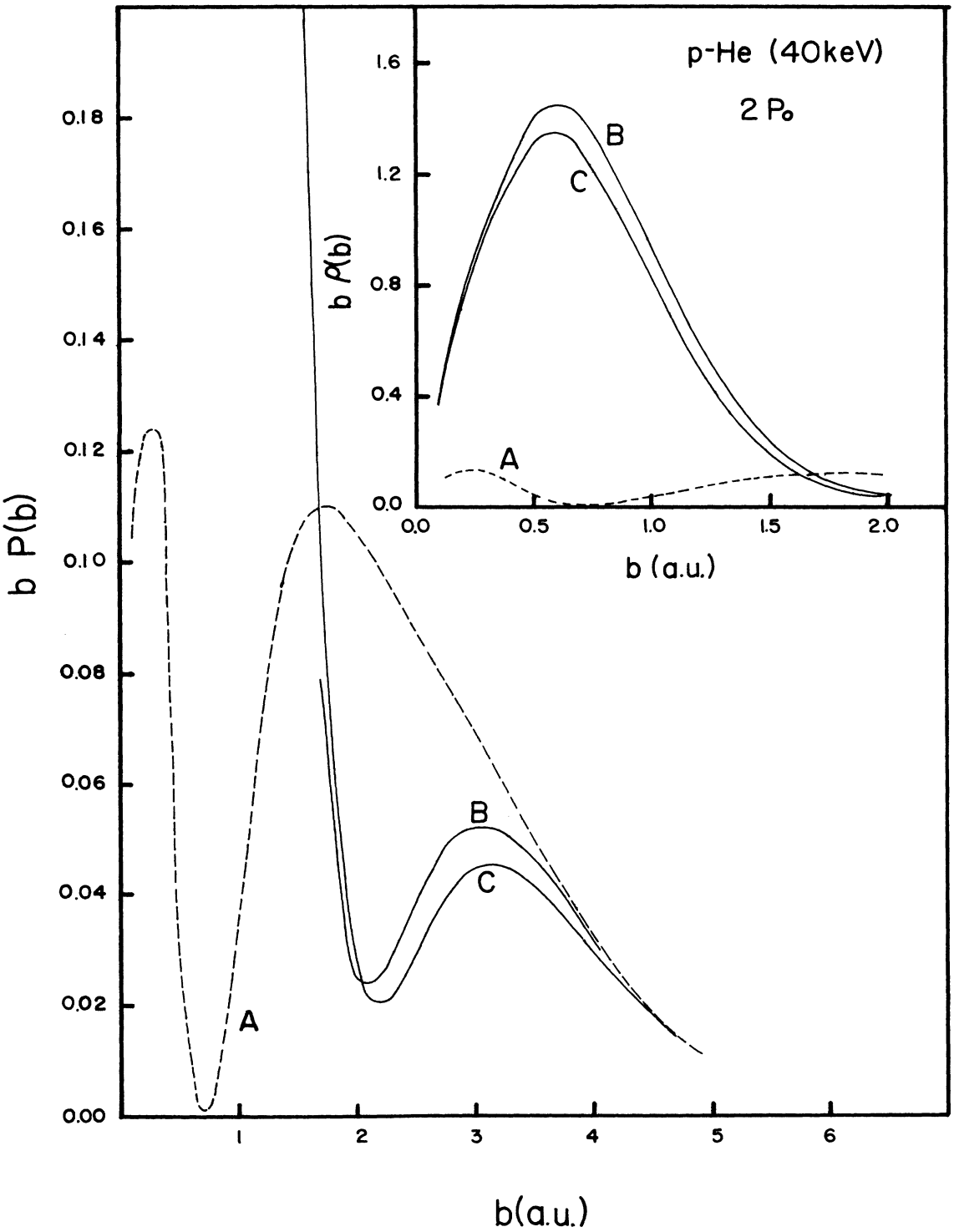

FIG. 2. Same as Fig. 1 except that the transfer probability is for the $2p_0$ state. The curves B are obtained in a 16-state basis set.

we have given the full basis set employed in the following calculations on both centers, including the corresponding energy eigenvalues. Thus, in the final calculations of the density matrices, a total number of 19 states was used in the AO+ expansion. The precise form of these pseudostates (Table I) is not crucial for the accuracy of the amplitudes[29] (see below for discussion).

As a standard procedure, the substitution of Eq. (3) into (2) results in a set of first-order coupled differential equations for the amplitudes $a_i^T(t)$ and $a_j^P(t)$, which are solved numerically (with proper initial boundary conditions) for each impact parameter b. We denote these amplitudes as a_{nlm}^P $(t=\infty;b)$ for a particular nlm excited state of the H atom at impact parameter b and at any given energy.

III. THE DENSITY MATRIX AND ITS FIRST-ORDER MOMENTS

In p + He collisions, excited states of the H atoms are populated at each impact parameter b and energy: The wave function of this pure state of the H atom for a particular n manifold can be described as

$$\bar{\Psi}_{nlm}(\mathbf{b};\mathbf{r})=a_{nlm}^P(t=\infty;b)\Phi_{nlm}(\mathbf{r}) , \tag{6}$$

where $\Phi_{nlm}(\mathbf{r})$ are hydrogen eigenfunctions. The b-dependent density matrix for a particular n manifold is given by (dropping the indexes P and $t=\infty$)

$$\rho_{nlm,nl'm'}(b)=a_{nlm}(b)[a_{nl'm'}(b)]^* \tag{7a}$$

and the integrated density-matrix elements are obtained by integrating Eq. (7a) over the impact-parameter plane, i.e.,

$$\bar{\rho}_{nlm,nl'm'}=\int_0^{2\pi}\int_0^{\infty}a_{nlm}(b)[a_{nl'm'}(b)]^* b\,db\,d\phi . \tag{7b}$$

Not all the elements of the density matrix in Eqs. (7a) and (7b) are nonzero. Symmetries in the collision allow only a certain number of nonzero matrix elements to occur. First, the density matrix is Hermitian, i.e.,

$$\rho_{nlm,nl'm'}(b)=[\rho_{nlm,nl'm'}(b)]^* , \tag{8a}$$

$$\bar{\rho}_{nlm,nl'm'}=(\bar{\rho}_{nlm,nl'm'})^* . \tag{8b}$$

Second, the reflection symmetry (with respect to the x-z plane) allows only elements to be nonzero for which

$$\rho_{nlm,n'l'm'}(b)=(-1)^{m+m'}\rho_{nl-m,nl'-m'}(b) , \tag{9a}$$

$$\bar{\rho}_{nlm,n'l'm'}=(-1)^{m+m'}\bar{\rho}_{nl-m,nl'-m'} . \tag{9b}$$

Third, in case of the integrated density matrix $\bar{\rho}$ [Eq. (7b)] the cylindrical symmetry further reduces the number of nonzero elements by requiring that

$$\bar{\rho}_{nlm,nl'm'}=\bar{\rho}_{nlm,nl'm'}\delta_{mm'} . \tag{10}$$

For example, the 9×9 density matrix [Eq. (7b)] for $n=3$ involves only ten independent quantities [six (real) diagonal and four (complex) off-diagonal, after considering the symmetry constraints of Eqs. (8)–(10)] to determine it completely. However, the b-dependent density matrix [Eq. (7a)] does not have the cylindrical symmetry and therefore the number of independent elements is larger. Notice that the magnitude of the diagonal elements is proportional to the cross section for the particular nlm sublevel, while the off-diagonal elements give the coherences or the average phase differences between these magnetic substates.

As mentioned earlier, the significance of the density matrix is found in terms of various physically meaningful parameters, which are derived from the real and imaginary parts of the off-diagonal matrix elements. The dipole moment vector for a particular n manifold is written as

$$D_n(b)=\sum_{\substack{l,m,\\ l',m'}}\int\bar{\Psi}_{nlm}(\mathbf{b};\mathbf{r})\mathbf{r}\bar{\Psi}_{nl'm'}(\mathbf{b};\mathbf{r})d\mathbf{r} , \tag{11}$$

where the hydrogenic eigenfunctions $\bar{\psi}_{nlm}$ are defined in Eq. (6). The averaged dipole moment is obtained by integrating Eq. (11) over all impact parameters and normalizing the corresponding number by the trace of the density matrix (total cross section for that particular principal quantum number n). Thus, for $n=2$ and 3 the $\langle D_z\rangle_{n=2}$ and $\langle D_z\rangle_{n=3}$ are given by

$$\langle D_z\rangle=6\,\mathrm{Re}(\bar{\rho}_{00,10})/\mathrm{Tr}(\bar{\rho}_{n=2}) , \quad n=2 \tag{12a}$$

and

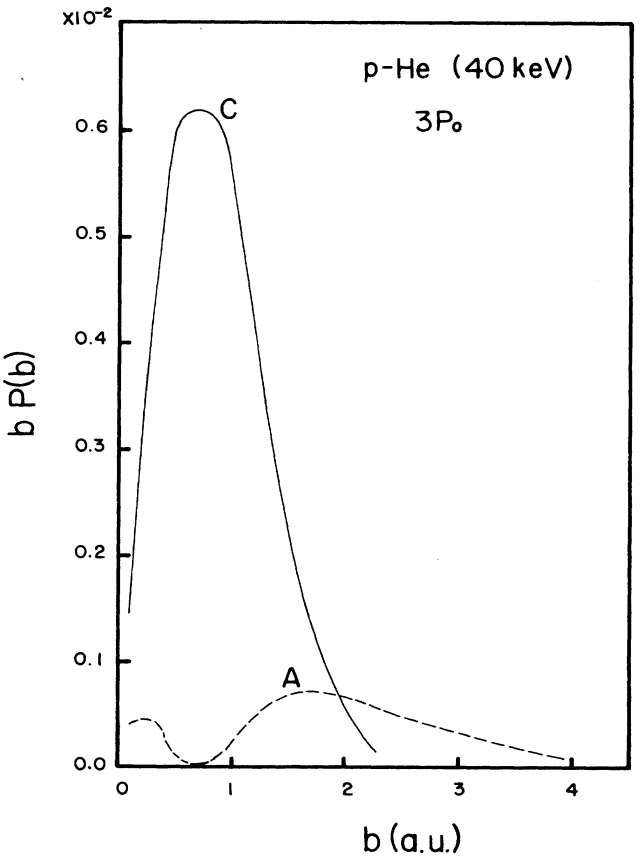

FIG. 3. Same as Fig. 1, but for the $3p_0$ capture channel.

$$\langle D_z \rangle = \frac{6\sqrt{6}}{\mathrm{Tr}(\bar{\rho}_{n=3})} \mathrm{Re}(\bar{\rho}_{00,10} + \sqrt{1/2}\bar{\rho}_{10,20} + \sqrt{3/2}\bar{\rho}_{11,21}) , \quad n=3 . \tag{12b}$$

An alternative interpretation of the coherences between the real parts of the off-diagonal matrix elements is provided by the electronic probability density function $\tilde{D}(\mathbf{r};b)$ (Ref. 18)

$$\tilde{D}(\mathbf{r};b) = \sum_{\substack{l,m,\\ l',m'}} \mathrm{Re}[\rho_{nlm,nl',m'}(b)\Phi_{nlm}(\mathbf{r})\Phi^*_{nl'm'}(\mathbf{r})] . \tag{13}$$

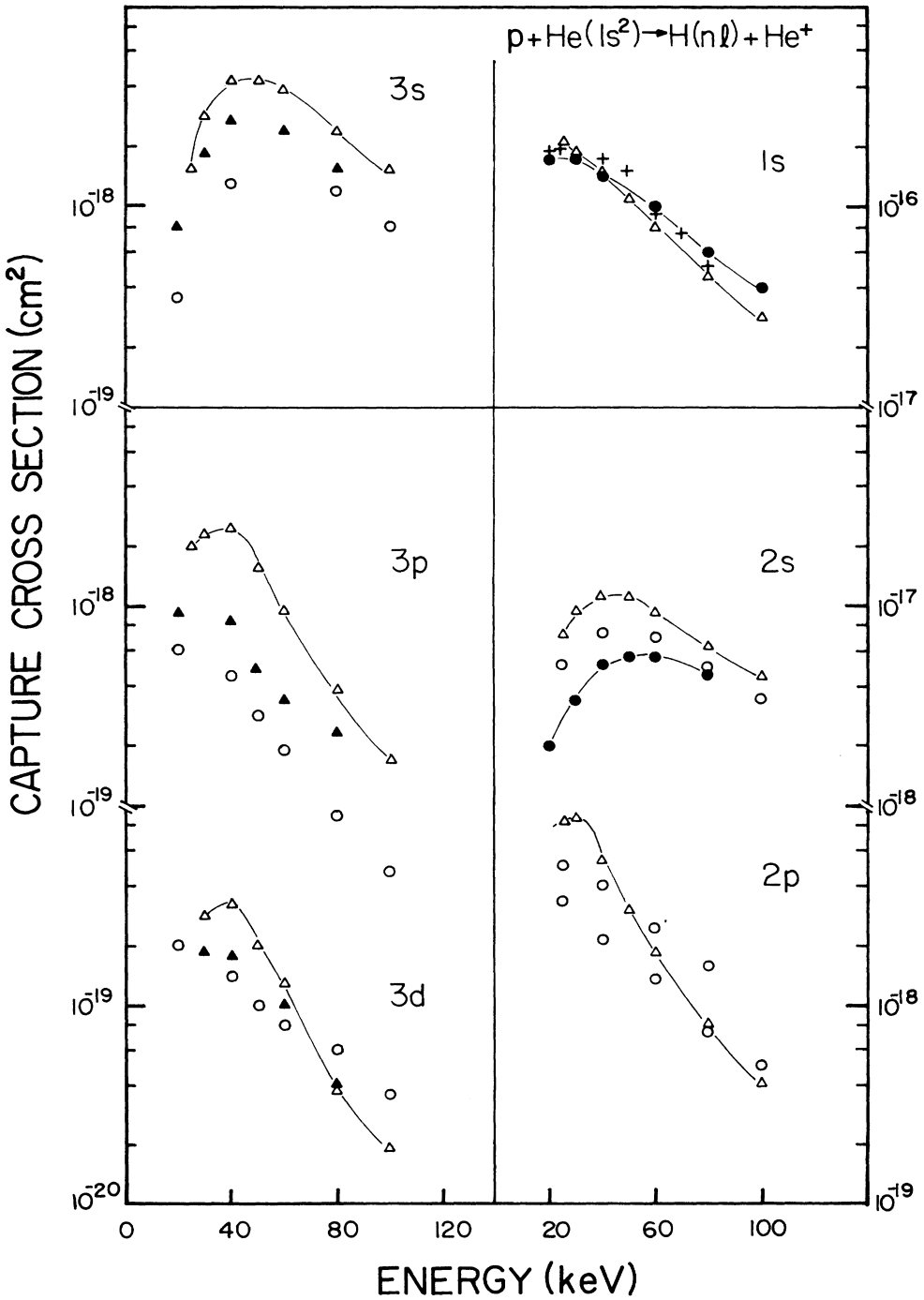

FIG. 4. Capture cross sections into the nl (1s, 2s, 2p, 3s, 3p, 3d) sublevels of hydrogen atoms at various energies. Theory: open triangles, present 19-state AO+ calculation; solid circles, AO-MO results of Kimura and Lin (Ref. 13). Experimental data are from Ref. 5 (open circles), Ref. 32 (plus signs), and Ref. 7 (solid triangles). Right-hand curves follow the right-hand scale.

In order to interpret the meaning of the coherences between the imaginary parts of the off-diagonal density-matrix elements, the vector $(\mathbf{L}\times\mathbf{A})$ is constructed from the angular momentum vector $\mathbf{L}$ and the Runge-Lenz vector $\mathbf{A}$ (which is proportional to the dipole moment vector). Classically, the vector $(\mathbf{L}\times\mathbf{A})$ points in the direction of the velocity of the orbiting electron around the projectile. Burgdorfer[24] has given explicit expressions for various first-order multipoles of the density matrix for any given n. The averaged z component of the vector $(\mathbf{L}\times\mathbf{A})$ is expressed for $n=3$ as[24]

$$\langle \mathbf{L}\times\mathbf{A}\rangle_{z,s}=\frac{4}{\mathrm{Tr}(\bar{\rho})}\sqrt{2/3}\,\mathrm{Im}(\bar{\rho}_{00,10}+\sqrt{2}\bar{\rho}_{10,20}+\sqrt{6}\bar{\rho}_{11,21}) \tag{14a}$$

TABLE II. Integrated density matrix (normalized to the $3s$ cross section) for $n=3$ manifold of excited H atoms formed in p-He collisions at 60 keV.

Element	Energy (keV) 25	30	35	40	50	60	80
s	1.0	1.0	1.0	1.0	1.0	1.0	1.0
p_0	0.97	0.607	0.667	0.512	0.334	0.232	0.139
		0.58[a]			0.19[a]	0.18[a]	0.13
				0.23[b]		0.22[c]	−0.09[b]
p_1	0.150	0.068	0.039	0.0268	0.0157	0.012	0.0118
		0.36[a]			0.08[a]	0.04[a]	0.05[a]
				0.11[b]		−0.014[c]	0.11[b]
d_0	0.22	0.057	0.073	0.064	0.04	0.03	0.012
		0.055[a]			0.017[a]	0.019[a]	0.013[a]
				0.00[b]		0.027[c]	0.04[b]
d_1	0.033	0.0197	0.011	0.0066	0.0033	0.0024	0.002
		0.046[a]			0.014[a]	0.014[a]	0.010[a]
				0.06[b]		−0.005[c]	0.03[b]
d_2	0.002	0.0008	0.0004	0.000 27	0.000 17	0.000 14	0.000 16
		0.022[a]			0.001[a]	0.002[a]	0.002[a]
				−0.01[b]		0.009[c]	−0.01[b]
$\mathrm{Re}(sp_0)$	0.480	0.520	0.529	0.480	0.362	0.270	0.130
				0.36[b]		0.33[c]	0.22[b]
$\mathrm{Re}(sd_0)$	0.220	0.209	0.229	0.202	0.137	0.110	0.0133
				0.18[b]		0.086[c]	0.18[b]
$\mathrm{Re}(p_0d_0)$	0.325	0.122	0.148	0.132	0.084	0.062	0.018
				0.09[b]		0.039[c]	0.02[b]
$\mathrm{Re}(p_1d_1)$	0.045	0.023	0.011	0.0086	0.0048	0.004	0.0034
				0.00[b]		0.00[c]	0.00[b]
$\mathrm{Im}(s_0p_0)$	−0.470	−0.520	−0.356	−0.306	−0.203	−0.134	−0.080
				−0.26[b]		−0.046[c]	0.01[b]
$\mathrm{Im}(s_0d_0)$	0.107	0.0083	0.026	0.022	0.022	0.02	0.0032
				−1.08[b]		−0.05[c]	−0.85[b]
$\mathrm{Im}(p_0d_0)$	−0.136	0.105	0.139	0.119	0.078	0.056	0.025
				0.00[b]		0.016[c]	0.00[b]
$\mathrm{Im}(p_1d_1)$	0.0538	0.0283	0.0153	0.0086	0.0048	0.0037	0.0034
				0.00[b]		0.002[c]	0.00[b]

[a]Reference 11 (expt.).
[b]Reference 18 (expt.).
[c]Reference 19 (expt.).

and for $n=2$

$$\langle \mathbf{L}\times\mathbf{A}\rangle_{z,s}=\frac{-2}{\mathrm{Tr}(\bar{\rho})}\mathrm{Im}(\bar{\rho}_{00,10}) . \quad (14b)$$

An alternative interpretation of the coherences between the imaginary parts of the off-diagonal elements is provided by the electronic current distribution,[18] namely,

$$j(\mathbf{r})=\sum_{\substack{l,m,\\ l',m'}} \mathrm{Im}[\bar{\rho}_{nlm,nl'm'}\Phi^{*}_{nl'm'}(\mathbf{r})\nabla\Phi_{nlm}(\mathbf{r})] . \quad (15)$$

In this paper we present dipole moment [Eq. (12)], velocity vector [Eq. (14)], and the probability distribution function [Eq. (13)] as function of impact parameter. This interpretation demonstrates a better picture of the charge-transfer process and the excited final states of the hydrogen atoms.

IV. RESULTS AND DISCUSSION

A. Calculation of the scattering amplitudes and the convergence of the AO+ basis set

In order to see the quality and the convergence of the present basis set, we first show in Figs. 1–3 the capture probability $P(b)$ (multiplied by b) at 40 keV for $2s$ (and $3s$), $2p_0$, and $3p_0$ channels, respectively, using AO+ basis sets with 19 [including seven pseudostates, namely, two UA orbitals on each center and three $2s$, $2p_0$, and $2p_1$ orbitals on the target (see Table I)] and 16 (without three extra $n=2$ terms on the target) terms. Also shown in these figures are the pure AO basis set (12-state) calculations without including any pseudostates. (In Figs. 1 and 3 we have not shown the 16-state curves, as they are very close to the 19-state curves.) As expected, the effect of UA orbitals is substantial in the small-b region. The capture probabilities calculated with 19- and 16-term sets is in qualitatively good agreement with each other. However, the 12-state AO curves are in great disagreement both in quality and quantity up to intermediate b values (3–4 a.u.).

Although the aim of the present work is to calculate and analyze the $n=2$ and 3 density matrices for the excited H atoms formed in $p+$He collisions, it is also worthwhile to report our total and partial capture cross sections, since there are no theoretical results available—for example, for the $3l$ subshell except in the first Born approximation by Mapleton.[31] In our final AO+ basis set we include only the $n=2$ excitation channel on the target. The agreement of the present $n=2$ He excitation cross section with experiment[32] and the other theoretical[13,33] calculations is qualitative for all the partial ($2s$, $2p_0$, and $2p_1$) cross sections: The maximum discrepancy is observed at higher energies ($E>50$ keV), where our values are larger by about a factor of 2.

There are several measurements on the partial nl ($n=2$ and 3) subshell cross sections for the $p+$He system in the present energy region.[5–11,34] In Fig. 4 we have displayed our $1s$, $2s$, $3s$, $2p$, $3p$, and $3d$ capture cross sections along with various experimental points.[5–8] Also shown in this figure are the AO-MO calculations of Kimura and Lin[13] for the $1s$, $2s$, and $2p$ capture channels only: These calculations have been extended up to an energy of 100 keV. It can be seen from Fig. 4 that the present AO+ results are in good harmony with experimental results although the available measured points themselves do not fully agree with each other. The importance of UA orbitals is clear at the lower end of the present energy range, where the 12-state results involve larger errors (not shown). In summary, we notice that there is qualitative agreement between theory and measurement for all the nl sublevels (Fig. 4). We shall not discuss further the nlm magnetic substates in this subsection since these cross sections appear as the diagonal parts of the full density matrix to be described in the next subsection.

B. Comparison of experimental and theoretical density matrices for the $n=2$ and 3 manifolds

We first consider the integrated density matrix for the $n=3$ manifold for which recent experimental data[18–19] are available for comparison. Although the experimental results for the density matrix have been presented in the full 40–80-keV energy region, most recent and improved data are available only at 60 keV.[19] On the other hand, the diagonal elements (partial cross sections for the individual nlm sublevels) of the $n=3$ density matrix have been measured recently[11] in the energy range 30–80 keV; these numbers, however, are measured in absolute units but normalized with respect to the $3s$ partial cross sections. In Table II we show the present values of the integrated density-matrix elements [Eq. (7)] at 25, 30, 35, 40, 50, 60, and 80 keV along with the experimental data[11,18–19] (only at 30 and 50, 40, 60, and 80 keV). It is clear from this table that the agreement between theory and experiment at all energies considered

TABLE III. Same as Table II, but for $n=2$ manifold.

	Energy (keV)							
Element	25	30	35	40	50	60	80	100
s	0.260	0.354	0.396	0.414	0.400	0.348	0.235	0.155
p_0	0.230	0.265	0.223	0.170	0.098	0.058	0.024	0.012
p_1	0.039	0.027	0.019	0.013	0.008	0.006	0.003	0.002
Re(sp_0)	0.129	0.172	0.159	0.133	0.091	0.059	0.024	0.01
Im(sp_0)	−0.132	−0.148	−0.136	−0.111	−0.063	−0.029	0.004	0.014

here is encouraging except for weaker channels, where the discrepancy between theory and experiment is significant. For the $n=2$ manifold, there are no experimental data available for comparison: Our present values of the $n=2$ integrated density matrices are displayed in Table III at 25, 30, 35, 40, 50, 60, 80, and 100 keV.

From the off-diagonal integrated density-matrix elements (Tables II and III), we now evaluate the z component (the x component is zero from symmetry properties) of the averaged dipole moment $\langle D_z \rangle$ [see Eq. (12)] and the velocity vector $\langle \mathbf{L}\times\mathbf{A} \rangle_{z,s}$ [Eq. (14)] normalized to the n manifold capture cross section. Figure 5 illustrates these parameters as a function of energy for both the manifolds $n=2$ and 3. The experimental values for $n=3$ $\langle D_z \rangle$ and $\langle \mathbf{L}\times\mathbf{A} \rangle_{z,s}$ at 40, 60, and 80 keV from Ref. 18 and more recent values only at 60 keV from Ref. 19 are also plotted in this figure. Also shown in Fig. 5 are the calculations for $n=3$ $\langle D_z \rangle$ and $\langle \mathbf{L}\times\mathbf{A} \rangle_{z,s}$ employing the continuum-distorted-wave (CDW) approximation [which includes postcollision interaction (PCI) also] from Ref. 22.

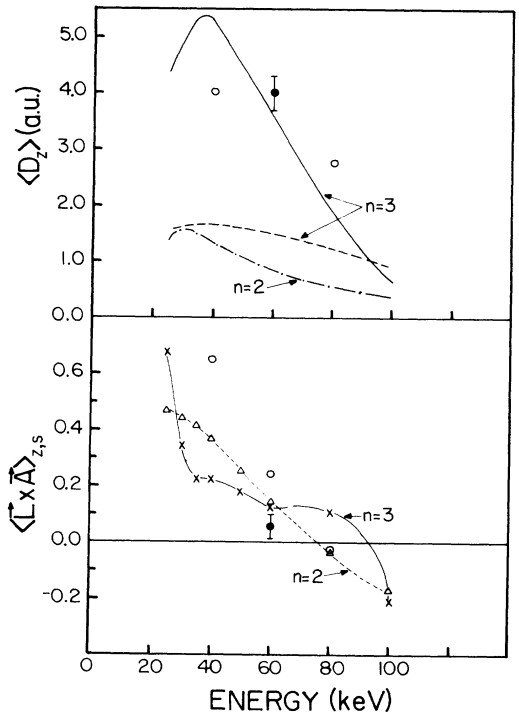

FIG. 5. Averaged dipole ($\langle D_z \rangle$) and $\langle \mathbf{L}\times\mathbf{A} \rangle_{z,s}$ moments for $n=2$ and 3 excited states of H atoms formed in 25–100-keV p-He charge-transfer collisions. Upper set of curves for $\langle D_z \rangle$: solid curve, present results for $n=3$; long dashed curve, CDW calculations of Ref. 22 for $n=3$; dash-dot curve, present $n=2$ manifold. Experiment points are for $n=3$ from Ref. 18 (open circles) and Ref. 19 (solid circles). Lower points are for the vector $\langle \mathbf{L}\times\mathbf{A} \rangle_{z,s}$: Present results for $n=3$ and 2 are shown by crosses and open triangles, respectively, while the corresponding experimental values for $n=3$ manifold at 60 keV (solid circles) are from Ref. 19 and at 40, 60, and 80 keV (open circles) are from Ref. 18.

Several interesting points are observed from Fig. 5: First, we note that there is good agreement between theory and most recent experimental[19] values of the dipole moment and the velocity vector at 60 keV; second, the CDW-PCI values[22] are too small below 80 keV (note that quantitatively the CDW theory may not be accurate in this energy region); and third, the $\langle D_z \rangle$ is positive throughout, while the velocity vector $\langle \mathbf{L}\times\mathbf{A} \rangle_{z,s}$ changes sign around 90 keV. This change of sign in the $\langle \mathbf{L}\times\mathbf{A} \rangle_{z,s}$ vector is also observed in the experimental study around 80 keV and also in the CDW (PCI) calculations of Burgdorfer.[22] The positive values of the dipole moment for both n values indicate that the electron cloud lags behind the projectile in the energy range considered here. At higher energies the dipole moment drops rapidly reflecting that capture to $3p$ and $3d$ states becomes relatively small compared with the $3s$ channel at these energies. For lower velocities, the dipole moment acquires a maximum value of 5.4 a.u. for $n=3$ at 35 keV and 1.55 a.u. for $n=2$ at 30 keV (the maximum value allowed in this case for $n=3$ is 7.5 a.u. and for $n=2$ is 3.0 a.u.). In Tables IV and V the values of $\langle D_z \rangle$ and $\langle \mathbf{L}\times\mathbf{A} \rangle_{z,s}$ are given at all energies.

The density matrix contains all the information extractable from scattering experiments. The $\langle D_z \rangle$ and $\langle \mathbf{L}\times\mathbf{A} \rangle_{z,s}$ moments discussed above are just two convenient parameters which offer some simple physical interpretation of the coherences between off-diagonal matrix elements. As mentioned earlier, the coherences between the off-diagonal matrix elements can be visualized in terms of probability density (due to real parts of the off-diagonal elements) and the current density (due to imaginary parts of the off-diagonal elements) functions.[17] Therefore, we have plotted three-dimensional graphs of integrated (over b) $\bar{D}(r)$ [Eq. (13)] for both the $n=2$ and 3 manifolds at selective energies of 35, 60, and 80 keV in Figs. 6 and 7, respectively. It is clear from these figures (6 and 7) that in both manifolds ($n=2$ and 3) the charge cloud lagging behind the projectile (which corresponds to positive values of the $\langle D_z \rangle$) is consistent with the results of Fig. 5. As the energy increases, the asymmetry in the charge distribution decreases (corresponding to a small $\langle D_z \rangle$ value). Note that the large peak at the projectile center is due to the dominant $3s$ component of the

TABLE IV. Values of the averaged z component of the normalized dipole moment $\langle D_z \rangle$ of the excited H atoms formed in p-He collisions (in atomic units).

	$n=3$		$n=2$
Energy (keV)	Theory	Expt. (Ref. 18)	Theory
25	4.37		1.36
30	4.90		1.54
35	5.37		1.45
40	5.23	4.00	1.31
50	4.45		1.06
60	3.62	3.55 (4.13[a])	0.85
80	1.83	2.75	0.55
100	0.66		0.35

[a]Most recent value supplied by Westerveld (Ref. 19).

TABLE V. Values (in atomic units) of the normalized $\langle \mathbf{L}\times\mathbf{A}\rangle_{z,s}$ vector for the captured electron in p-He collisions as a function of impact energy.

Energy (keV)	Present theory $n=2$	Present theory $n=3$	Experiment (Ref. 18) $n=3$
25	0.465	0.674	
30	0.439	0.330	
35	0.413	0.223	
40	0.365	0.226	0.648
50	0.247	0.187	
60	0.138	0.118	0.24 (0.05[a])
80	−0.033	0.105	−0.025
100	−0.168	−0.212	

[a]Most recent value supplied by Westerveld (Ref. 19).

$\bar{D}(r)$. The asymmetric ridges in the forward and the backward direction are produced mainly by the off-diagonal elements between states of opposite parity, which give rise to an electric dipole moment [see Eq. (12)]. It is interesting to notice that the patterns seen in Figs. 6 and 7 are qualitatively similar for the excited states of the H atoms in the $n=2$ and 3 shells, except the fact that the $n=3$ graphs (Fig. 6) have two asymmetric regions: the second asymmetry (at larger negative z distances) in the $n=3$ density matrix, which is absent in the $n=2$ case (Fig. 7), comes mainly from the s-d and p-d coherences. However, the major contribution to the $\langle D_z\rangle$ comes from the dominant s-p mixing.

As discussed earlier, the vector $\langle \mathbf{L}\times\mathbf{A}\rangle_{z,s}$ [Eq. (14)]

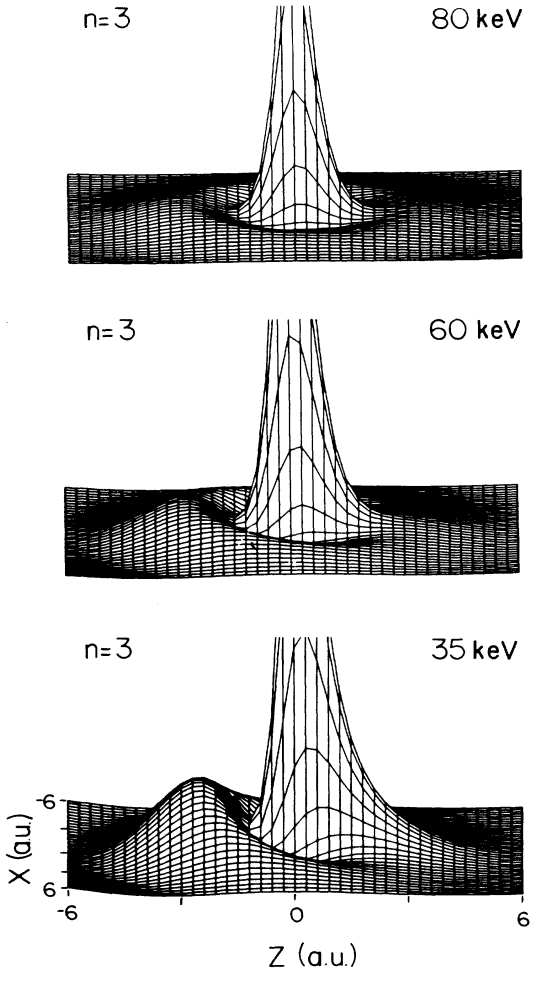

FIG. 6. Electron probability distribution for hydrogen ($n=3$) atoms formed in p-He collisions at 35, 60, and 80 keV.

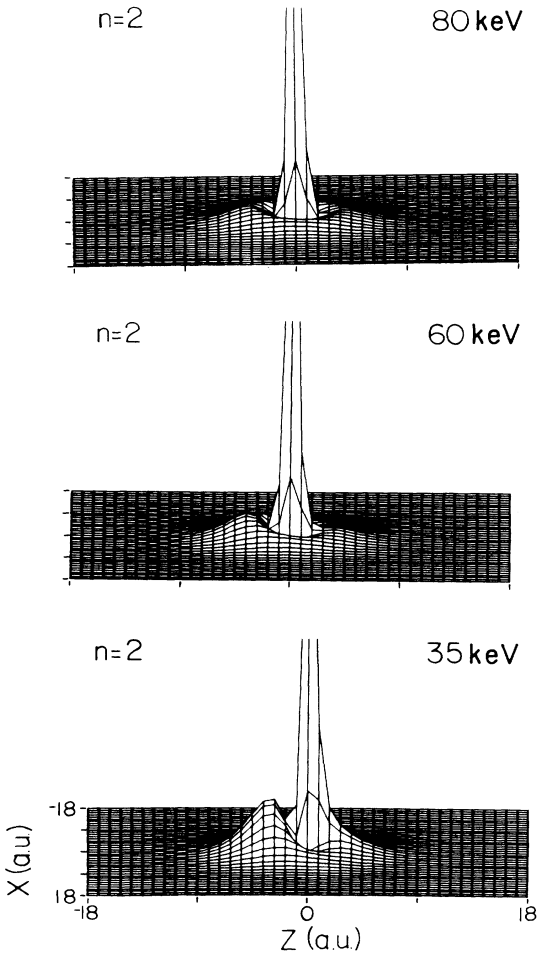

FIG. 7. Same as Fig. 6, but for $n=2$ manifold.

is a quantum-mechanical quantity which, in a classical sense, is a measure of the z component of the velocity vector of the captured electron at the projectile. We noticed from Fig. 5 that the $\langle \mathbf{L}\times\mathbf{A}\rangle_{z,s}$ changes sign (direction) between the energies 80–100 keV. Alternatively, this property can be demonstrated by the current density [Eq. (15)] contour plots as illustrated in Fig. 8. Here, we have plotted $j(\mathbf{r})$ in the collision plane (x-z) at 35, 60, 80, and 100 keV energies. Clearly this Fig. 8 indicates that above 80 keV, the direction of the current reverses, which is consistent with the sign changeover of vector $\langle \mathbf{L}\times\mathbf{A}\rangle_{z,s}$ in Fig. 5. The flow pattern of three energies (35, 60, and 80 keV) are similar, while for the 100-keV graph, it changes significantly.

To understand the results of Figs. 6–8 it is necessary to examine the impact-parameter dependence of the density matrix and its parametrization. In this case the cylindrical symmetry no longer exists and density-matrix elements with $m-m'\neq 0$ are nonzero. We can therefore calculate the x component (the y component is still zero due to reflection symmetry with respect to the x-z collision plane) of the dipole moment $[D_x(b)]$. This means that the probability density functions should reveal asymmetric patterns along the x axis also. First, we display in Figs. 9 and 10, for the $n=3$ and 2 manifolds, the decomposition of the dipole moment $D(b)$ (both x and z components) at 35 and 60 keV energies, respectively. Notice that the quantities in Figs. 9 and 10 are not normalized (with respect to the trace of the density matrix).

We learn from Figs. 9 and 10 that $D_z(b)$ is positive at all impact parameters indicating that the center of the electron cloud always lags behind the projectile at all b values [which is true for other energies also (not shown)]. For $D_x(b)$, however, we see that there is a sign change. At large b, $D_x(b)$ is positive, while it is negative for intermediate values of impact parameters [contribution

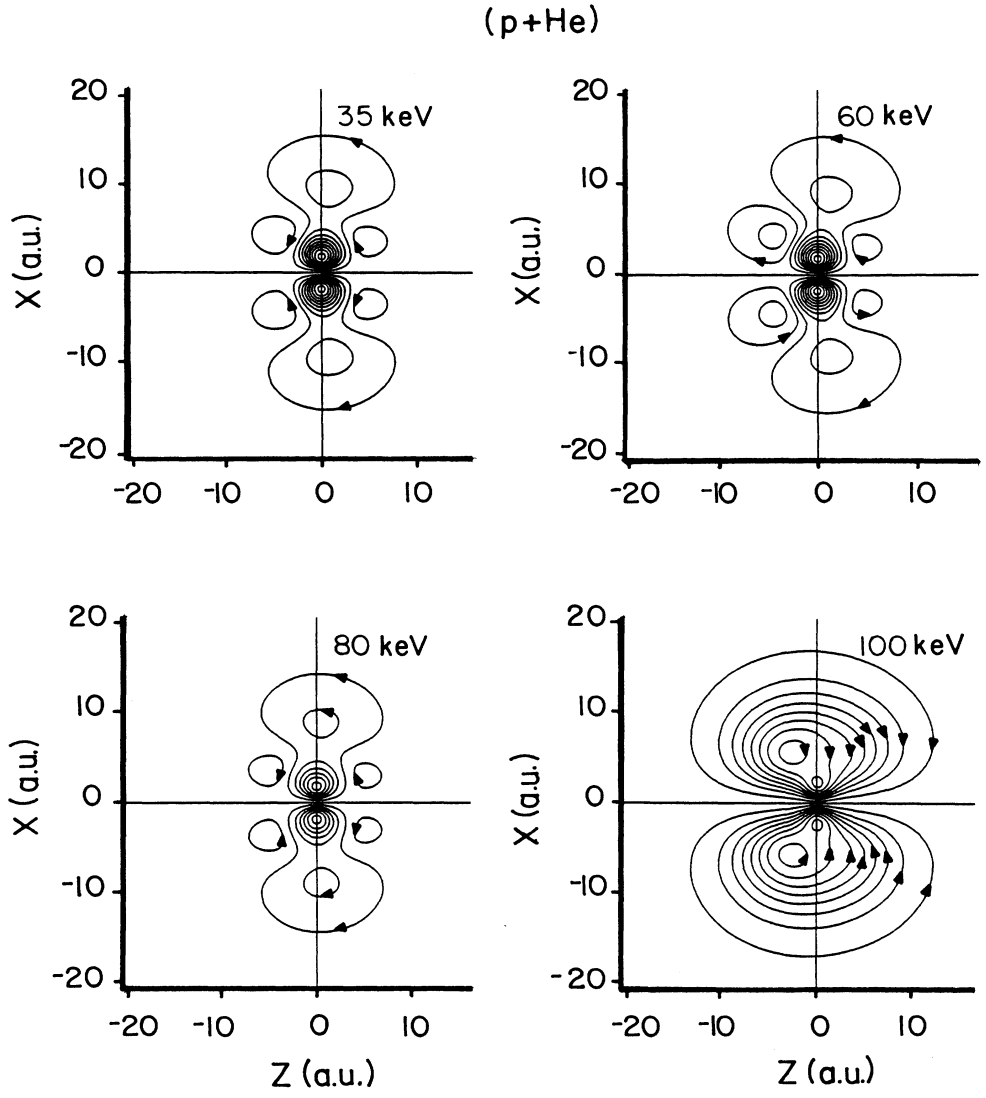

FIG. 8. Electronic current flow diagram of the H($n=3$) atoms emerging from p-He collisions at 35, 60, 80, and 100 keV energies. The flow lines separate equal flows weighted by the distance from the z axis, i.e., equal amounts of $(x^2+y^2)^{1/2}j$.

from very small b (<0.5 a.u.) values are negligible]. This is true for other energies (25, 30, 35, 40, 80, and 100 keV) also (not shown). We notice from Figs. 11 and 12 that the behavior of both manifolds is very similar, which also indicates that the $3d$ state does not affect the qualitative features of the transfer mechanism (it may be interesting to compare $n=2$ and $n=3$ manifolds in those situations where the $3d$ state is important).

We now show the differential charge cloud distribution at several impact parameters for both manifolds. Figures 11 and 12 present the $n=3$ density distribution three-dimensional graphs at $b=0.5$, 1.3, 2.5, and 3.7 values (in a.u.) for two representative energies 35 and 60 keV, respectively. In complete agreement with Figs. 9 and 10, the asymmetry in the x direction suggests that the x component of the dipole moment reverses direction at large b values: The sign of the $D_x(b)$ is positive at $b=2.5$ and 3.7, while at other b values these density plots show that the $D_x(b)$ is negative. Note that each graph is normalized separately in order to display its structure more clearly. In Fig. 13, for $n=2$ manifold, as an example, we have shown the differential probability function only for 35 keV at $b=1.3$, 2.5, and 3.7 a.u. It is quite clear from this figure that at $b=1.3$ a.u., the $D_x(b)$ is negative, while at the other two b values it is certainly positive in complete agreement with Fig. 9. The discussion of this paragraph is true at other energies also (not shown). We also note from Figs. 11 and 12 that the p-d and s-d coherences manifest themselves at large distances (secondary peaks) although the s-p coupling dominates giving rise to strong peaks in the density function near the origin. The d coherences are zero in the case of $n=2$; therefore no such large distance peaks are seen in $n=2$ plots (Fig. 13).

The z component of the differential vector $(\mathbf{L}\times\mathbf{A})_{z,s}$ is displayed in Fig. 14; its value is positive for small b and negative for large b; this changeover of sign in its b dependence in fact illustrates that the electronic charge and current distributions at the end of the collision are quite different at small and large impact parameters.

The present b-dependent expectation values of the dipole $[D(b)]$ and velocity vectors $[\mathbf{L}\times\mathbf{A}(b)]$ may now be explored to present a classical picture of the captured electron in the coherently excited n manifold. This picture is equivalent to a differential experiment with detection of the scattering angle of the outgoing projectile in the x-z collision plane. By reflection symmetry, only two components of each vector $D_x(b)$, $D_z(b)$ and $(\mathbf{L}\times\mathbf{A})_z(b)$, $(\mathbf{L}\times\mathbf{A})_x(b)$ can have nonzero values. This can be viewed as a "classical" Kepler orbit in the x-z plane with the angular momentum (L_y) pointing in either $+y$ direction depending on the rotational sense. Note that this type of classical orbital picture is not defined in the integral experimental situation where all the transverse components vanishes. The classical picture emerging from our differential expectation values of the dipole and velocity vectors is depicted in Fig. 15 for small and large b values. The Kepler orbits of the cap-

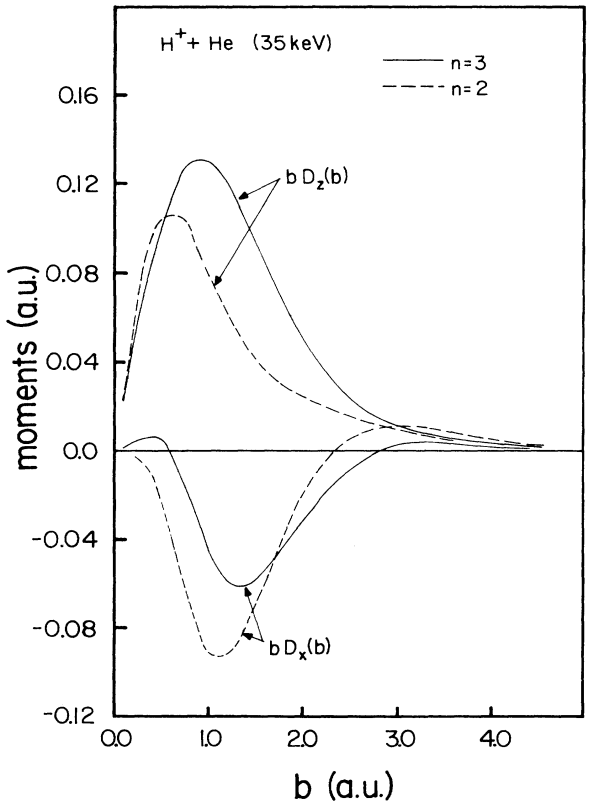

FIG. 9. Calculated impact-parameter-dependent dipole vector $D(b)$ (x and y components) at 35 keV. $n=3$, solid curves; $n=2$, dashed curves.

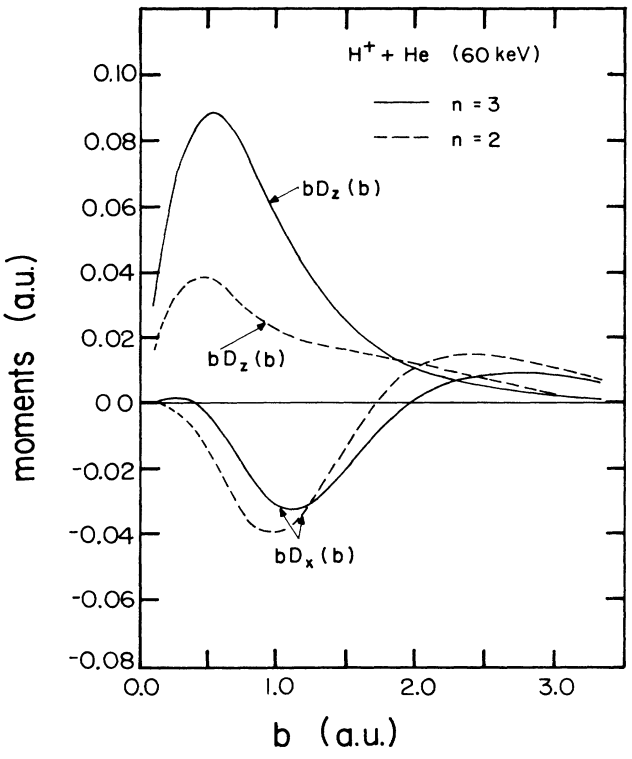

FIG. 10. Same as Fig. 9, but at 60 keV.

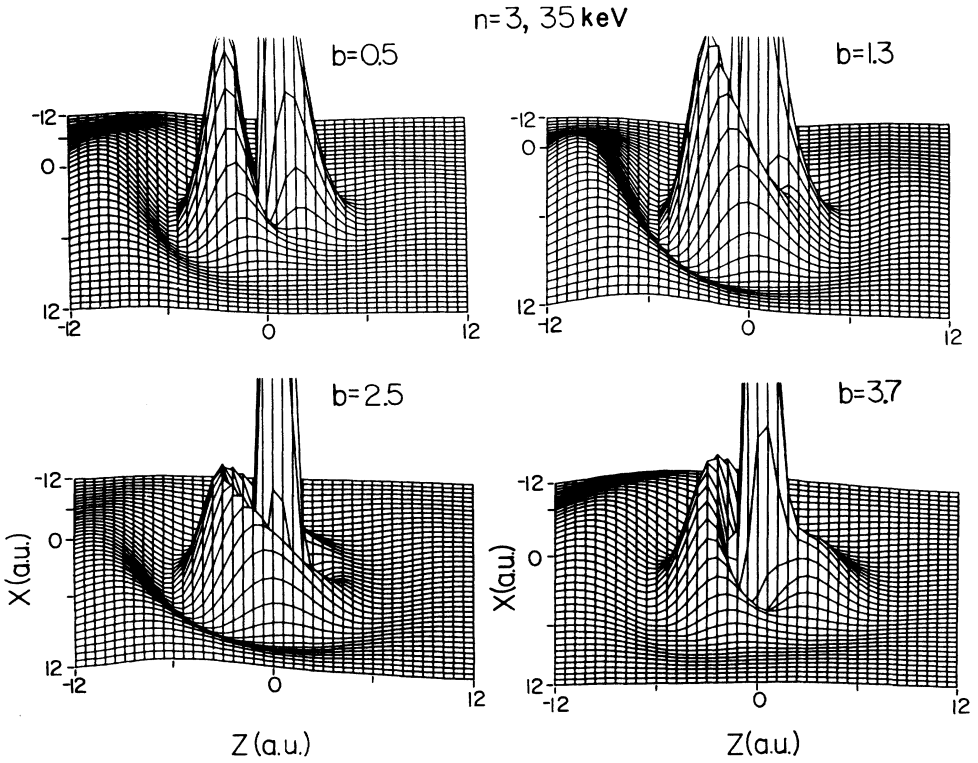

FIG. 11. b-dependent probability density of the charge cloud of H($n=3$) atoms formed in p-He collisions at 35 keV. Note that each plot is weighted arbitrarily in order to expose its hidden structures.

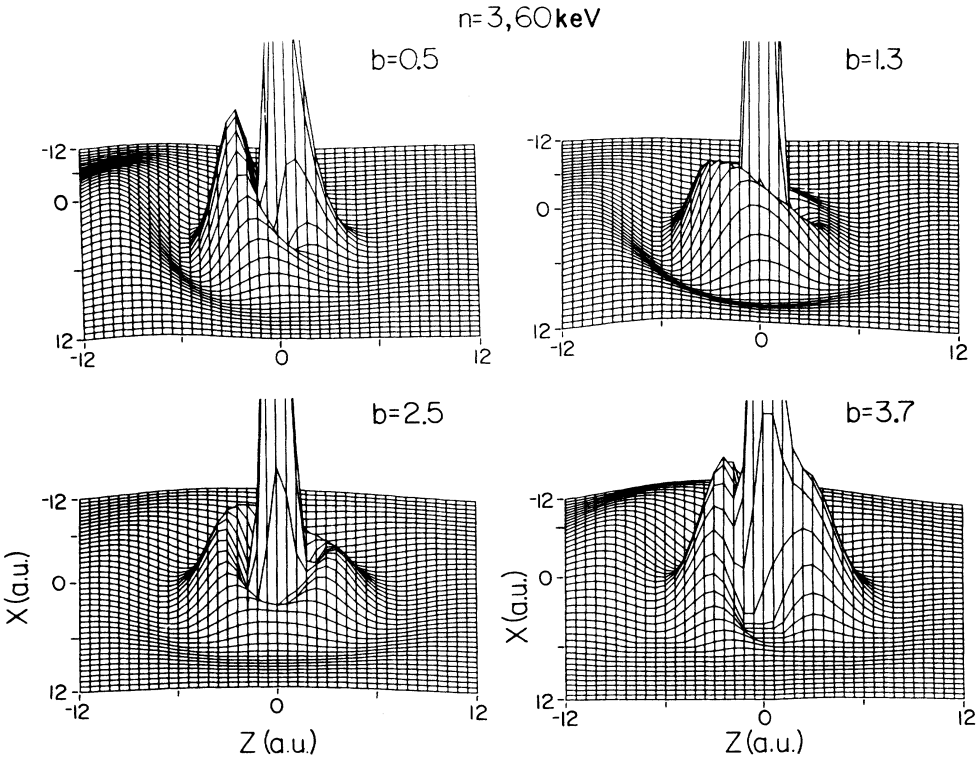

FIG. 12. Same as Fig. 11 except at 60 keV.

tured electron, consistent with the calculated D_x, D_z, and $(\mathbf{L}\times\mathbf{A})_{z,s}$, are shown in Fig. 15(a) for small b and in Fig. 15(b) for large b values. Notice that the speed of the electron is slowest at the aphelion and fastest at the perihelion and that the $(\mathbf{L}\times\mathbf{A})_{z,s}$ is in the direction of the orbital velocity at the perihelion.

In Fig. 15(a) the orbit is oriented such that it gives a positive D_z and a negative D_x and the arrows indicating the orbiting direction of the electron are consistent with positive $(\mathbf{L}\times\mathbf{A})_{z,s}$. In contrast, the orbit and the sense of rotation in Fig. 15(b) correspond to a positive D_z, a positive D_x, and a negative $(\mathbf{L}\times\mathbf{A})_{z,s}$. The above classical Kepler orbits are consistent with a simple intuitive picture of electron capture. At large impact parameters, due to short interaction time, we can expect that the electron is pulled towards the projectile throughout the collision time; thus the electron lags behind the projectile nucleus and lies between the two heavy particles. On the other hand, for collisions at small b values, the electron has to swing back toward the projectile as it overshoots to the right during the early stage of the collision.

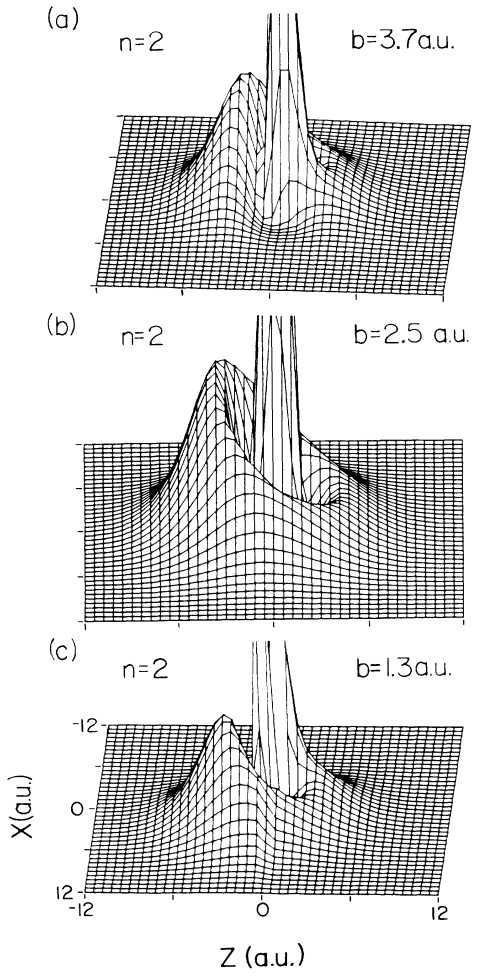

FIG. 13. Same as Fig. 11 except for the $n=2$ manifold and at 35 keV.

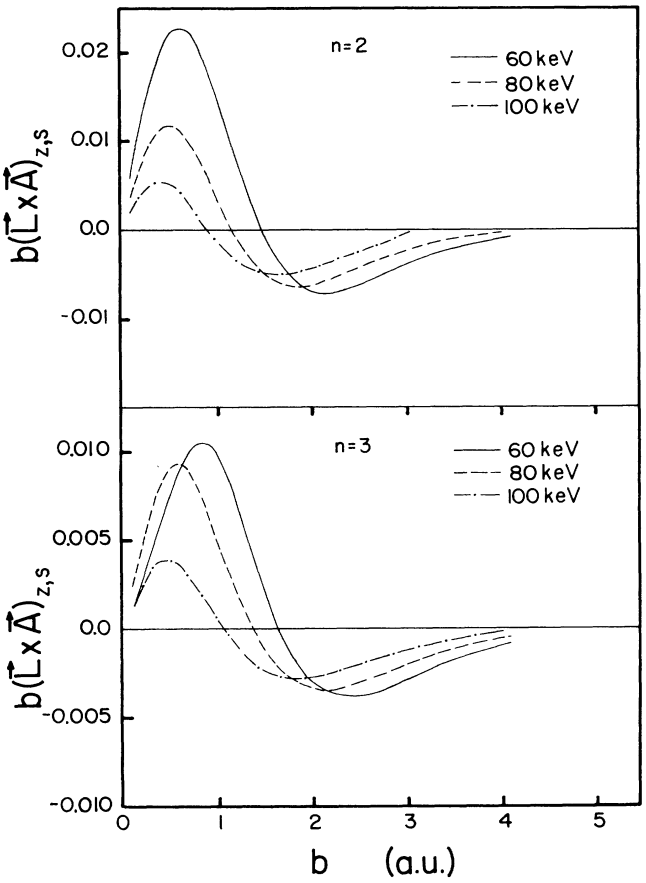

FIG. 14. Vector $(\mathbf{L}\times\mathbf{A})_{z,s}$ as a function of impact parameter for both the manifolds ($n=2$ and 3) at 60, 80, and 100 keV energies.

V. CONCLUSIONS

We computed full density matrices for the excited H atoms in $n=2$ and 3 shells formed in p-He charge-transfer reaction at intermediate velocities. The corresponding charge-transfer scattering amplitudes were determined in the two-center AO+ model in which the usual atomic-orbital basis is augmented with extra orbitals (so-called pseudostates) taking approximately into account the effects of excitation and ionization channels at higher energies and large impact parameters and also the effects of molecular features in the small impact region at the lower end of the present energy region. The resulting nl-subshell partial cross sections were found in agreement with available experimental and other theoretical results.

From the integrated (over impact parameters) density-matrix elements, several physical quantities (such as the dipole moment, velocity vector, probability and current densities, etc.) were calculated and compared with existing experimental numbers. On the average, we agree with almost all features observed in the experimentally determined density-matrix elements by Havener *et al.*[16–18] and Westerveld:[19] for example, the fact that

the electronic charge cloud lags behind the proton and that the flow of current patterns changes direction above 80 keV impact energy. Although the determination of 14 density-matrix elements from experimental observations is very difficult and more refined values of these elements and moments have become available recently,[19] it is very unlikely that the qualitative features discussed so far will get changed by the new updated data. On the other hand, it would be very interesting if the $n=2$ manifold were measured. This should pose less limitations in extracting the density-matrix elements which are now only five instead of 14 as in case of the $n=3$ manifold. However, it would require a different optical detecting system.

The differential density matrix is calculated here for the first time. By analyzing the b-dependent dipole moments and velocity vector ($\mathbf{L}\times\mathbf{A}$), we have been able to provide a simple classical picture of the averaged electron density and current distributions after the capture. It would be interesting if differential experiments were performed in the future.

We have made a similar density-matrix analysis for the prototype p-H one-electron system.[35] It is observed that at somewhat lower energies ($E \leq 10$ keV) the average dipole moment ($\langle D_z \rangle$) is negative. More experimental work and better theoretical models are needed in order to fully understand the charge-transfer mechanism.

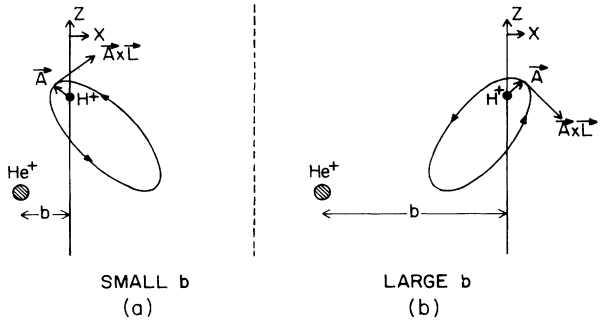

FIG. 15. A classical orbital picture of the captured electron in (a) small-b and (b) large-b regions.

ACKNOWLEDGMENTS

We thank J. Risley, W. Westerveld, C. C. Havener, M. Brower, and J. Burgdorfer for stimulating discussions and for sending us their data prior to publication. We are also thankful to William Westerveld for allowing us to use his program to make the plots of Fig. 8. This work was supported in part by the U.S. Department of Energy, Office of Energy Research, Division of Chemical Sciences.

[1]H. R. Dawson and D. H. Loyd, Phys. Rev. A **15**, 43 (1977).
[2]M. B. Shah, J. Geddes, and H. B. Gilbody, J. Phys. B **13**, 4049 (1980).
[3]D. H. Crandall and D. H. Jaecks, Phys. Rev. A **4**, 2271 (1971).
[4]R. H. McKnight and D. H. Jaecks, Phys. Rev. A **4**, 2281 (1981).
[5]R. H. Hughes, E. D. Stokes, J. Song-sik Choe, and T. J. King, Phys. Rev. A **4**, 1453 (1971); this paper gives earlier references also.
[6]J. L. Edwards and E. W. Thomas, Phys. Rev. A **2**, 2346 (1970).
[7]J. Lenormand, J. Phys. (Paris) **37**, 699 (1976).
[8]J. C. Ford and E. W. Thomas, Phys. Rev. A **5**, 1694 (1972).
[9]R. Hippler, W. Harbich, M. Faust, H. O. Lutz, and L. J. Dube, J. Phys. B **19**, 1507 (1986).
[10]R. Hippler, W. Harbich, H. Madeheim, M. Kleinpoppen, and H. O. Lutz (unpublished).
[11]M. C. Brower and F. M. Pipkin, Bull. Am. Phys. Soc. **31**, 994 (1986); M. C. Brower (private communication).
[12]M. Kimura, Phys. Rev. A **31**, 2158 (1985).
[13]M. Kimura and C. D. Lin, Phys. Rev. A **34**, 176 (1986).
[14]K. Blum, *Density Matrix Theory and Applications* (Plenum, New York, 1981).
[15]U. Fano and J. Macek, Rev. Mod. Phys. **45**, 553 (1973).
[16]C. C. Havener, W. B. Westerveld, J. S. Risley, N. H. Tolk, and J. C. Tully, Phys. Rev. Lett. **48**, 926 (1982).
[17]C. C. Havener, N. Rouze, W. B. Westerveld, and J. S. Risley, Phys. Rev. Lett. **53**, 1049 (1984).
[18]C. C. Havener, N. Rouze, W. B. Westerveld, and J. S. Risley, Phys. Rev. A **33**, 276 (1986).
[19]W. B. Westerveld (private communication).
[20]C. Dahaes and W. Singer, Phys. Lett. **75A**, 276 (1980).
[21]I. A. Sellin, J. R. Mowat, R. S. Peterson, P. M. Griffin, R. Laubert, and H. H. Haselton, Phys. Rev. Lett. **31**, 1335 (1973).
[22]J. Burgdorfer and L. J. Dube, Phys. Rev. Lett. **52**, 2225 (1984).
[23]G. Gabrielse and Y. B. Band, Phys. Rev. Lett. **45**, 553 (1973).
[24]J. Burgdorfer, Z. Phys. A **309**, 285 (1983).
[25]See, for example, C. D. Lin, Comments At. Mol. Phys. **11**, 261 (1982).
[26]A. Jain, C. D. Lin, and W. Fritsch, Phys. Rev. A **35**, 3180 (1987).
[27]D. G. M. Anderson, M. J. Antal, and M. B. McElroy, J. Phys. B **7**, L118 (1974); see also T. G. Winter and C. D. Lin, Phys. Rev. A **29**, 567 (1984).
[28]W. Fritsch, C. D. Lin, and L. N. Tunnell, IEEE Trans. Nucl. Sci. **NS-28**, 1146 (1981); W. Fritsch and C. D. Lin, J. Phys. B **16**, 1595 (1983).
[29]W. Fritsch and C. D. Lin, Phys. Rev. A **27**, 3361 (1983).
[30]L. Opradolce, P. Valiron, and R. McCarroll, J. Phys. B **16**, 2017 (1983).
[31]R. A. Mapleton, Phys. Rev. **122**, 528 (1961).
[32]T. J. Kvale, D. G. Seely, D. M. Blankenship, E. Redd, T. J. Gay, M, Kimura, E. Rille, J. L. Peacher, and J. T. Park, Phys. Rev. A **32**, 1369 (1985).
[33]M. R. Flannery, J. Phys. B **3**, 306 (1970).
[34]J. B. H. Stedeford and J. B. Hasted, Proc. R. Soc. London, Ser. A **227**, 466 (1955).
[35]A. Jain, C. D. Lin, and W. Fritsch (unpublished).